A&A 393, 43–56 (2002)
DOI: 10.1051/0004-6361:20020906

Astronomy
&
Astrophysics

Near-IR 2D-spectroscopy of the 4″× 4″ region around the Active Galactic Nucleus of NGC 1068 with ISAAC/VLT★

E. Galliano and D. Alloin

European Southern Observatory, Casilla 19001, Santiago, Chile

Received 17 October 2001 / Accepted 13 June 2002

Abstract. New near-IR long slit spectroscopic data obtained with ISAAC on VLT/ANTU (ESO/Paranal) complement and extend our previously published near-IR data (Alloin et al. 2001) to produce Br_γ and H_2 emission line maps and line profile grids of the central 4″ × 4″ region surrounding the central engine of NGC 1068. The seeing quality together with the use of an 0.3″ wide slit and 0.3″ slit position offsets allow one to perform 2D-spectroscopy at a spatial resolution ≈ 0.5″. Slit orientations (PA = 102° and PA = 12°) were chosen so as to match respectively the equatorial plane and the axis of the suspected molecular/dusty torus in NGC 1068. The selected wavelength range from 2.1 to 2.2 μm is suitable to detect and analyze the Br_γ and H_2 emission lines at a spectral resolution corresponding to 35 km s^{-1}. An asymmetric distribution of H_2 emission around the continuum peak is observed. No H_2 emission is detected at the location of the strong 2.2 μm continuum core (coincident within error-bars with the central engine location), while two conspicuous knots of H_2 emission are detected at about 1″ on each side of the central engine along PA = 90°, with a projected velocity difference of 140 km s^{-1}: this velocity jump has been interpreted in Alloin et al. (2001) as the signature of a rotating disk of molecular material. From this new data set, we find that only very low intensity Br_γ emission is detected at the location of the two main knots of H_2 emission. Another knot with both H_2 and Br_γ emission is detected to the North of the central engine, close to the radio source C where the small scale radio jet is redirected and close to the brightest [OIII] cloud NLR-B. It has a counterpart to the South, placed almost symmetrically with respect to the central engine, although mainly visible in the Br_γ emission. The northern and southern knots appear to be related to the ionization cone. At the achieved spectral resolution, the H_2 emission line profiles appear highly asymmetric with their low velocity wing being systematically more extended than their high velocity wing. A simple way to account for the changes of the H_2 line profiles (peak-shift with respect to the systemic velocity, width, asymmetry) over the entire 4″ × 4″ region, is to consider that a radial outflow is superimposed over the emission of the rotating molecular disk. We present a model of such a kinematical configuration and compare our predicted H_2 emission profiles to the observed ones. Excitation of the H_2 line is briefly discussed: X-ray irradiation from the central engine is found to be the most likely source of excitation. Given the fact that the material obscuring our direct view toward the central engine is Compton thick ($N_\mathrm{H} \geq 10^{24}$ cm^{-2}), the observed location of the main H_2 knots at a distance of 70 pc from the central engine suggests that the rotating molecular disk is warped.

Key words. galaxies individual: NGC 1068 – galaxies: Seyfert – galaxies: nuclei – galaxies: active – infrared: galaxies – molecular data

1. Introduction

Over the past decade, considerable efforts has been devoted to a better understanding of active galactic nuclei (AGN). In particular, the use of HST (UV and visible ranges), the use of adaptive optics (AO) on 4 m-class telescopes (near-IR range) and the use of interferometry (millimeter and radio ranges) have brought a large gain in spatial resolution and hence many new constraints for AGN modeling. Conversely, the so-called unified model (see Krolik 1999) has played an important role in stimulating the search for AGN constituents: in particular for the elusive pc-scale molecular/dusty torus which is thought to surround the central engine (black hole and accretion disk) and to funnel the ionizing radiation within a cone. Models of the infrared (IR) emission of the torus published so far, have explored torus radii from 1 to 100 pc (Krolik & Begelman 1986; Pier & Krolik 1993; Granato & Danese 1994; Efstathiou & Rowan-Robinson 1994; Granato et al. 1997), while the thickness, composition and inclination of the torus are other key-parameters in the modeling. Given the input energy distribution from the central engine, models then predict the flux spatial distribution at IR wavelengths from 2.2 μm up to 20 μm in the central 100 pc region of the AGN. If one chooses an AGN for which the spatial resolution reachable today (typically 0.1″ with the facilities mentioned above in a range from UV to millimetric) provides an intrinsic scale relevant to the torus size, a comparison between predicted IR maps and observed ones will be an excellent opportunity for deriving stringent constraints on the model parameters. This calls for investigating a close-by and torus-inclined AGN: NGC 1068 is an ideal target.

Send offprint requests to: E. Galliano,
e-mail: `egallian@eso.org`

★ Based on observations collected at the ESO/Paranal 8 m UT1 telescope, Proposals 63.P-0167A & 66.B-0142A.

This galaxy is located at a distance of 14.4 Mpc, assuming a Hubble constant of 75 km s^{-1} Mpc^{-1}. The corresponding scale is 70 pc per arcsec. Many high resolution images have indeed been obtained over the past decade: decisive contributions come from the HST in the UV, visible (Capetti et al. 1997) & near-IR (Thompson et al. 2001), from AO in the near-IR (Marco et al. 1997; Thatte et al. 1997; Rouan et al. 1998; Marco & Alloin 2000), using shift-and-add techniques or diffraction-limited observations on 8 m class telescopes in the mid-IR (Bock et al. 2000; Tomono et al. 2001), from millimeter interferometry (Helfer & Blitz 1995; Tacconi et al. 1997; Baker 2000; Schinnerer et al. 2000) and radio interferometry (Gallimore et al. 1997). In this paper, we consider the compact radio source S1 (nomenclature after Gallimore et al. 1996) as the nuclear reference, that is the central engine location. Several observational facts suggest the presence of a molecular/dusty torus in NGC 1068. The term torus is used here in the sense of a rotating disk-like distribution. From inner to outer scales, let us point out the most relevant ones:

- The 1 pc-size disk of ionized material seen almost edge-on at PA = 110°, within S1, which has been detected at 8.4 GHz with the VLBA: it is thought to trace the inner walls of the torus (Gallimore et al. 1997)
- The core and the 15 pc-size elongated structure (at PA = 102°), detected at 2.2 μm with CFHT AO/PUEO (Rouan et al. 1998) and also present on 3.5 and 4.5 μm images with ESO AO/Adonis (Marco & Alloin 2000); the position of the near-IR core is found by Marco et al. (1997) to be coincident with S1 within ±0.05″. This configuration is consistent with thermal emission from dust particles at 1500 K in the core, and 600 K at a radius of 15 pc and could trace the body of the torus.
- From interferometer maps (Baker 2000; Schinnerer et al. 2000) one observes, in addition to a yet unresolved core of low level CO emission, two prominent CO emitting peaks located symmetrically 1″ (70 pc) away from S1 at PA = 98° and separated in velocity by 100 km s^{-1}: the authors interpret the CO observed emission in terms of a warped CO disk.

The possible presence of a molecular/dusty torus could be unveiled through the analysis of the H$_2$ roto-vibrational v = 1–0 S(1) emission line at rest wavelength 2.122 μm. Indeed, excitation of molecular transitions such as H$_2$ 2–1 S(1) and H$_2$ 1–0 S(1) can occur from irradiation by UV photons or X-rays, as well as from shocks, all ingredients which are found in profusion in an AGN. In addition, as the H$_2$ emission arises from warm molecular gas, the study of the H$_2$ lines provides physical information complementary to that derived from CO molecular transitions.

Molecular hydrogen was detected for the first time in an extragalactic source in the central region of NGC 1068 by Thompson, Lebofsky & Rieke (1978). They also detected Br$_\gamma$ emission in this region. Further H$_2$ line observations were carried out by Hall et al. (1981), and Oliva & Moorwood (1990). The first attempt at resolving spatially the H$_2$ emitting region was made by Rotaciuc et al. (1991): from their best-seeing map they found that the H$_2$ line emission was very weak at the location of the central engine and was mainly arising from two knots of unequal intensity located at ∼1.3″ from the nucleus along PA = 70°. A second attempt to get a ≤1″ resolution image in the H$_2$ line emission was made by Blietz et al. (1994). In the latter study, in contrary to Rotaciuc et al. (1991), the H$_2$ emission was found to arise in three knots, the brightest one being coincident (within an error bar of ±0.3″) with the strong near-IR continuum core (central engine location).

In this study, we analyze the H$_2$ and Br$_\gamma$ emission lines, at respective rest wavelengths 2.122 and 2.166 μm using ISAAC on VLT/ANTU, in its short wavelength medium resolution mode. Preliminary results about the H$_2$ emission within a small region (1.5″ × 1.5″) around the central engine were already published in a Letter (Alloin et al. 2001). In the current paper we extend the size of the region explored to 4″ × 4″ around the nucleus and provide H$_2$ line profiles and H$_2$ line emission maps over this region. We also analyze, similarly to H$_2$, the Br$_\gamma$ line emission map and line profiles. From the H$_2$ line profile analysis, we build a kinematical model of the warm molecular component in the AGN of NGC 1068.

We present in Sect. 2 the relevant information for data collection and data processing. In Sect. 3 we provide complete sets of the H$_2$ and Br$_\gamma$ line profiles across the entire region explored. From these data sets, emission maps in the H$_2$ and Br$_\gamma$ lines have been reconstructed and are compared to the map in the near-IR continuum. Fluxes and velocities are also given in Sect. 3. From the H$_2$ line peak velocities and profiles, we discuss in Sect. 4 the kinematics of the molecular material and we present in Sect. 5 a simple kinematical model, aiming at reproducing the profile shapes. Possible sources of excitation of the H$_2$ line in the close environment of the AGN in NGC 1068 are discussed in Sect. 5. Our concluding remarks are presented in Sect. 6.

2. Data: Collection and reduction

2.1. Instrumental setup

Observations were performed using the SWS1 short wavelength arm of ISAAC, in medium resolution mode (MR), attached to VLT/ANTU. Due to the request for very good seeing quality, observations were performed in service mode. Results discussed in this paper are based upon data acquired in July and August 1999, December 2000, and January and February 2001. A summary of the observations is given in Table 1. The slit width was set to 0.3″ while its length was of 2′. The slit was successively positioned at PA = 102° and PA = 12°. The orientation PA = 102° corresponds to the orientation of the trace of the torus suggested by the near-IR observations of Rouan et al. (1998), where we consequently expect to detect with maximum amplitude the velocity signature of a rotation. At the perpendicular orientation, PA = 12°, no rotational signature is to be expected. The slit positions were chosen to cover a spatially continuous area around the nucleus. Figure 1 shows the slit positions, superimposed over the AO M band image from Marco & Alloin (2000).

The spectral resolution of the MR mode is 8700 which, at 2.15 μm, translates into a 35 km s^{-1} resolution. The projected

Table 1. Summary of the observations.

date	PA	positions	average seeing(*)
99/08/01	102°	0.6″S,0.3″S,0.0″,	0.5″
		0.3″N,0.6″N	0.5″
99/09/17	12°	0.0″,0.3″W,0.6″W	0.45″
00/12/13	12°	0.3″E,0.6″E	0.75″
00/12/14	102°	0.9″S,1.2″S,1.5″S	0.9″
01/01/06	12°	0.9″E,1.2″E	0.37″
01/02/07	12°	1.5″E	0.55″

(*) Seeing values provided in this table have been taken from the ISAAC instrumental log. We have independently checked these values on the processed images wherever the slit was crossing through the nuclear unresolved K continuum source.

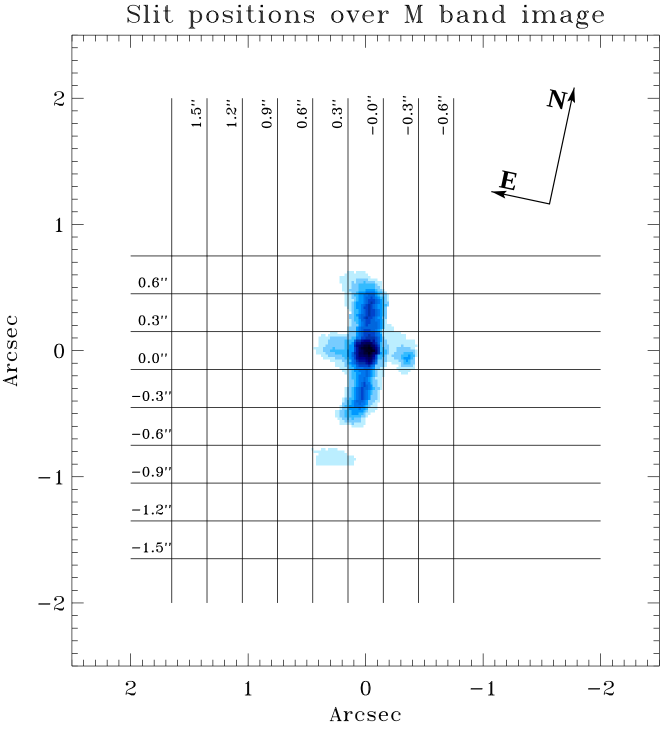

Fig. 1. Slit positions superimposed over the M band image from Marco & Alloin (2000). Horizontal figures are along PA = 102° while vertical ones are along PA = 12°.

scale on the detector is 0.147″ per pixel. Working in the IR, we used a standard nodding technique (408 pixels throw). The on-source individual exposure time is 270 s. Total integration times are in the range from 2×270 s to 6×270 s. The signal-to-noise ratio of the continuum reaches 100. Standard stars were acquired through 0.3″ and 2.0″ wide slits in order to respectively correct for sky absorption features and calibrate the data in flux.

2.2. Data reduction

Successive reduction steps were applied using the `IRAF` package, except for the electrical ghost removal, for which `Eclipse` was used. Details on IR spectra reduction and especially on the nodding technique (differential comparison A - B and B - A) can be found in the ISAAC data reduction manual, Cuby et al. (2000). The main steps are the following:

(1) correction of the electrical ghost: using the `Eclipse` is_ghost routine,

(2) simultaneous dark, bias and sky emission line subtraction: following the standard nodding technique,

(3) flat-field division: carried out after correction of the illumination variation along the slit,

(4) correction of 2D distortions (slit curvature and imperfect parallelism of the dispersion direction with the detector rows) using `IRAF`,

(5) correction of emission line residuals (see nodding technique),

(6) extraction of the spectra,

(7) wavelength calibration using the night-sky emission lines. The wavelengths are taken from the night-sky spectral atlas of OH emission lines in the near-IR by Rousselot et al. (2000),

(8) correction of the sky absorption lines: using spectra of standard stars,

(9) flux calibration performed using stellar models found in the "stellar spectra library" (`http://www.eso.org/instruments/isaac/lib/index.html`).

As we were interested in the spatial distribution of the line emission, we extracted a series of 1D-spectra from each 2D-spectrum: 3 pixels-high i.e. (0.45″ along the slit height) with a sliding step of 1 pixel (0.147″). The final spectral resolution is 2.5 Å, and the wavelength calibration sharp enough to measure the position of the night-sky lines within a precision of 0.1 Å. Over the central 0.3″×0.3″ area, the continuum is quite intense and produces a fringing pattern at the level of 5% (peak-to-peak) which cannot be fully corrected. This is the region where the H_2 line is weak or absent.

3. Data: Measurements and results

3.1. The H_2 and Br_γ emission: intensity maps

In each 1D-spectrum we measured the total velocity-integrated fluxes in the H_2 and Br_γ lines above the continuum. These measurements allowed us to reconstruct 2D maps of these line emissions. Figure 2 compares two reconstructed maps in H_2, obtained independently from the data sets at both PAs. On the left panel, the map reconstructed from the data set at PA = 12° has been overlaid on top of the map reconstructed from the data set at PA = 102°. The seeing value indicated relates to the PA = 12° spectrum through the intense H_2 knot to the East of the central engine (indicated by a cross). On the right panel, the map reconstructed from the data set at PA = 102° has been overlaid on top of the map reconstructed from the data set at PA = 12°, and the indicated seeing is for the PA = 102° spectrum through the H_2 knot to the East. The consistency of results derived from independent spectral data sets and the accuracy of the map reconstruction technique are successfully tested through the similarity of the structures appearing on both maps. The impact of a better image quality is also obvious in the left panel of Fig. 2 where the strongly emitting East-H_2 knot appears more sharply, as the seeing value was then down to 0.37″. Four particular regions are highlighted in Fig. 2, identified and discussed in Sect. 4.1. These are the East-H_2 knot, the North-H_2-Br_γ knot, the West-H_2 knot and the South-Br_γ knot, denominated according to their major line contribution.

The ISAAC H_2 map can be compared to the early map presented in Rotaciuc et al. (1991), within the limitation of different spatial resolutions. Considering only their H_2 image obtained under the best seeing conditions (Fig. 2 in their paper), we find indeed that their results are consistent with the ISAAC reconstructed maps, both in terms of positioning of the H_2 knots identified and in terms of their relative intensity. On the contrary, the H_2 line map presented by Blietz et al. (1994) is very different from that by Rotaciuc et al. (1991) and from the current ISAAC data set. While almost no H_2 line is found at the location of the near-IR continuum core, either by Rotaciuc et al. (1991) or from the ISAAC data, this is the strongest H_2 emission knot found by in Blietz et al. (1994) – in addition to the other H_2 knots which are in reasonable agreement with those detected by Blietz et al. (1994) and in the ISAAC data set. How could we explain this discrepancy? As the near-IR continuum core is very strong indeed, an extremely careful continuum subtraction is mandatory if one uses narrow-band imaging. The observed difference in H_2 line emission at the position of the continuum core, could easily be understood if the continuum had not been subtracted properly in the Fabry-Perot data set by Blietz et al. (1994), leaving a residual as a fake H_2 line emission.

Before discussing the ISAAC maps in detail, it is important to assess the level of the uncertainties in positioning and flux measurements.

3.2. Estimation of the error-bars in positioning and flux measurements

As mentioned above, we extracted from the 2D-spectra series of 1D-spectra through 0.45″(3 pixels along the slit) × 0.3″(slit width) windows, with a sliding step of one pixel (0.15″) along the slit. Each 1D-spectrum is assigned to a pseudo pixel on the reconstructed image. Hence, the pseudo pixel size is 0.3″(slit width) × 0.15″(sliding step along the slit), that is three times smaller than the extraction window. This is equivalent to applying a median filter to an image made of independent pixels. Each 2D-spectrum enables to reconstruct an 0.3″ wide strip of the final reconstructed image. These independent strips have to be carefully positioned along the direction of the slit with respect to a common reference position. Along each slit, the reference is set to the spectrum with maximum near-IR continuum level. We have checked that this positioning procedure works fine, using an acquisition image of the continuum in K. For cuts along either PA = 102° or PA = 12°, we find that the near-IR continuum maxima are located within an 0.3″ box around the intersection of the cut direction and its perpendicular passing through the core. This indicates that the relative positioning of the strips with respect to the core is precise within better than 0.3″. Moreover, as the telescope offsets are set with a precision greater than ±0.05″ and as the slit is 0.3″ wide, in the worst case, any identified structure on the reconstructed map has its coordinate perpendicular to the slit known better than within an 0.3″ window. In conclusion, any feature on the reconstructed images can be positioned with respect to the core within a box 0.3″ × 0.3″.

Regarding flux uncertainties, let us recall that the line fluxes are measured from the reconstructed line maps. To derive these maps we have combined spectra obtained under slightly different image quality: this introduces an uncertainty in the flux measurement, especially when measuring line fluxes from small scale structures on the image or from features with steep spatial intensity gradients. Actually, this effect is minimized here for the following reason: we have measured the velocity-integrated H_2 line flux in the East-H_2 knot, where the intensity gradient is steep, from a set of combined spectra all obtained under extremely good seeing (0.37″). In the other identified knots with H_2 line emission, West-H_2 knot and North-H_2-Br_γ knot, the intensity gradient is not as steep and then the effect of slight image quality differences not important. On the other hand, the great advantages of our technique over using direct images acquired through filters centered on the lines of interest are first, that the continuum subtraction is very precise and second, that we avoid any loss of line emission resulting from an unknown and unexpected velocity field of the emitting material, since the line profile is accessible. Therefore, the final precision on flux measurements depends on the flux calibration step itself which, in this wavelength domain and given the very good observing conditions, is expected to be better than 10%.

3.3. Line flux measurements and comparison with previous measurements

We provide in Table 2 the measured line fluxes in H_2 and Br_γ of the structures identified in Fig. 2, East-H_2 knot, West-H_2 knot, North-H_2-Br_γ knot and South-Br_γ knot. The "apertures" used to measure the fluxes are shown by the boxes sketched in Fig. 2. It should be noted that the exposure time indicated in the headers of files related to the ISAAC observations of July and August 1999 are incorrect. Consequently, the flux measurement in the H_2 line published by Alloin et al. (2001) is higher than the real value by a factor 6. The correct flux values are those given in the present paper. This error in the headers of ISAAC data files has been corrected for data taken after March 2000, but remains so far in the headers for data prior to this date. This will be modified in the future. Considering the flux calibration uncertainty (±10%) and the possible slight flux losses due to seeing effects and estimated to be less than 5%, we get a final flux precision of around ±10%.

For comparison with previously published measurements, those are recalled in Table 3. The dispersion in the H_2 and Br_γ line fluxes measured by various groups is large and there appears to be a monotonic decrease with time. At least two reasons can be invoked to explain the spread: (a) aperture differences and (b) intrinsic variability of the AGN in NGC 1068. Regarding the second point, it is well established that the near-IR continuum luminosity of the AGN in NGC 1068 has

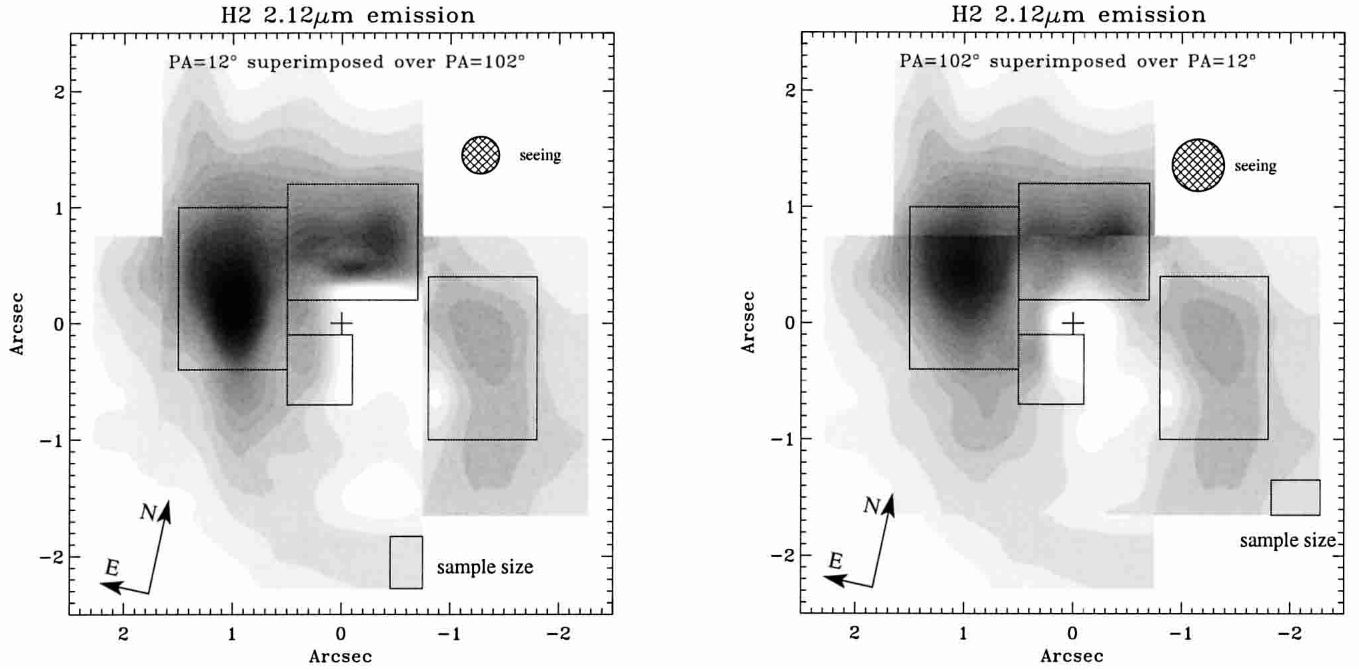

Fig. 2. Comparison between the H_2 maps reconstructed using the independent data sets at PA = 102° and PA = 12°. The seeing value given on each figure corresponds to the seeing value while the slit was crossing the intense eastern H_2 emitting knot. The maps have been rebinned to a smaller square-pixel to allow easier comparison between maps which have originally rectangular and differently oriented pixels. Similar structures appear on both maps. The impact of a better image quality on the sharpening of structures is also obvious. We show as well on these maps the spatial areas over which the total H_2, and if applicable Br_γ, line fluxes have been measured and given in Table 2. These are, starting from the box to the East, and turning clock-wise: the East-H_2 knot, the North-H_2-Br_γ knot, the West-H_2 knot and the South-Br_γ knot (see Sect. 4.1 for a detailed discussion). The location of the central engine is shown by a cross.

been increasing steadily since 1974 (Marco & Alloin 2000; Glass 1997). However, notice that the H_2 line emission is arising from regions located at least 40 pc away from the central engine (North-H_2-Br_γ knot): these regions are today in a state of excitation corresponding to the level of activity of the central engine about 100 years ago. Conversely, the near-IR continuum luminosity is known to arise from a core less than 0.12″ (8 pc) according to Rouan et al. (1998) or even as small as 0.03″ (0.02 pc) according to speckle measurements by Wittkowski et al. (1998): it may have increased over the past 25 years, without impacting yet on the H_2 line emission. This may explain the observed decoupled behaviour between the near-IR continuum flux and H_2 line time variations. Would well-sampled light-curves be available in the near-IR continuum and H_2 line, then time-delay effects could be used indeed to probe in another way the size of the H_2 line emitting region (e.g. Peterson 1994). We have measured as well the continuum value at 2.18 μm on the ISAAC spectra passing through the core. Taking into account the measured seeing (*FWHM* of a cut through the continuum), considering two values for the intrinsic core size of respectively 0.12″ and 0.2″ *FWHM*, and given the 0.3″ slit width, we have computed the corresponding slit losses. The final values for the flux of the core continuum at 2.18 μm are respectively 2.06×10^{-10} and 2.16×10^{-10} erg s^{-1} cm^{-2} μm^{-1}, for an 0.12″ and 0.2″ *FWHM* core. The value derived by Rouan et al. (1998) from AO observations of the unresolved core in *K* was of 0.8×10^{-10} erg s^{-1} cm^{-2} μm^{-1}.

Table 2. Line fluxes for the identified knots.

Source	Aperture center	Aperture size	H_2 line flux
East-H_2	+1.0″,+0.3″	1.0″ × 1.4″	2.3±0.3
West-H_2	-1.3″,-0.3″	1.0″ × 1.4″	0.7±0.1
South-H_2	0.2″,-0.4″	0.8″ × 0.8″	0.15 ± 0.05
North-H_2-Br_γ	-0.1″,+0.7″	1.2″ × 1.0″	1.3±0.2
Total	0″,0″	4.0″ × 4.0″	6.1±1.0
Source	Aperture center	Aperture size	Br_γ line flux
East-H_2	+1.0″,+0.3″	1.0″ × 1.4″	0.25 ± 0.15
West-H_2	-1.3″,-0.3″	1.0″ × 1.4″	< 0.2
South-H_2	0.2″,-0.4″	0.8″ × 0.8″	0.4 ± 0.1
North-H_2-Br_γ	−0.1″, +0.7″	1.2″ × 1.0″	2.8 ± 0.5
Total	0″,0″	4.0″ × 4.0″	5.2±1.0

Note: The flux unit is 10^{-14} erg s^{-1} cm^{-2}. The apertures are shown in Fig. 2; the aperture centers are defined with reference to the position of the K band unresolved core, coincident – within error-bars – with the radio source S1 (coordinates J2000 RA = 02 42 40.7098, Dec = −00 00 47.938 after Bland-Hawthorn et al. 1997). Be aware that the uncertainty on this positional reference is around 0.1″.

3.4. The H_2 and Br_γ emission: line profiles

Figures 3 and 4 provide respectively grids of the H_2 and Br_γ line profiles. In each box across this grid, we sample the

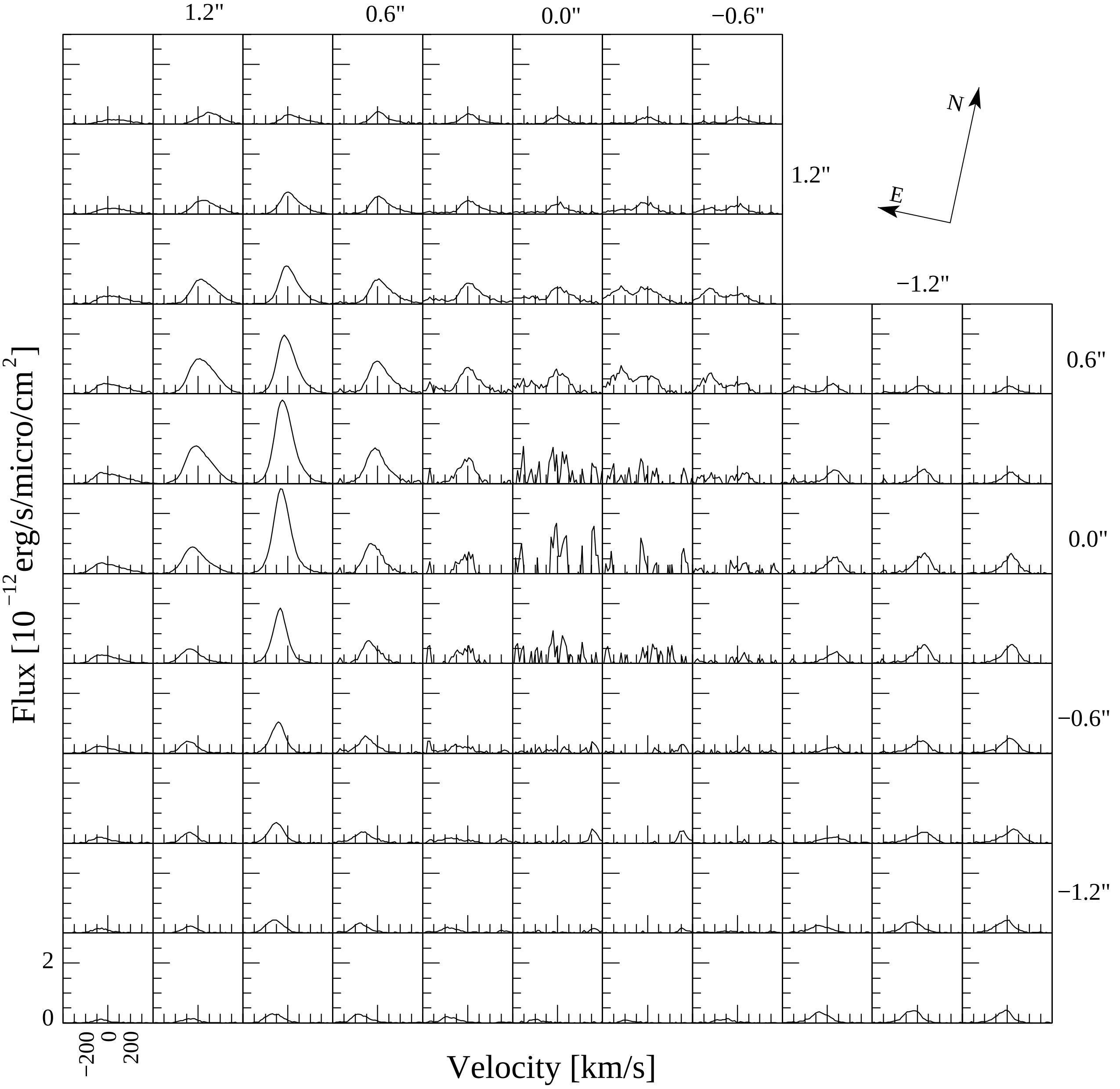

Fig. 3. The H_2 emission line profiles across the 3″ × 3″ region around the nucleus. North is up, East is left. Each box corresponds to an emitting region of 0.45″ × 0.3″. The unresolved continuum core in the K band is located at (0.0″,0.0″). The X-axis corresponds to PA = 102° and the Y-axis to PA = 12°. The velocity scale of the profile is shown on the bottom left of the X-axis. The intensity scale is displayed on the bottom left of the Y-axis.

Table 3. Previously published fluxes in the H_2 and Br_γ lines.

Author	Aperture	H_2 flux	Br_γ flux
Hall (1981)	3.8″ diam.	16.5	18.5
Oliva (1990)	6″ diam.	15. ± 1	13. ± 2
Rotaciuc (1991)	≈3″ diam.	8.6	4.
this paper (2002)	total ≈ 3″ diam.	6.1 ± 1.0	5.2 ± 0.5

The flux unit is 10^{-14} erg s^{-1} cm^{-2}. If not mentioned, the error-bars were not provided by the authors.

line profile and flux from an 0.3″ × 0.45″ sub-area. The X-axis provides its offset along PA = 102° (close to East-West) and the Y-axis its offset along PA = 12° (close to North-South). Positive coordinates along both axes are respectively to the East and North. The unresolved continuum core in the K band is referenced at coordinates (0.0″,0.0″). Regarding the central −0.3″ to +0.3″ strip, the strong near-IR continuum from the core induces a residual fringing level (3%) and a noise level which prevent measuring weak H_2 line emission. Given the mean seeing value (0.5″ in the K band), line profiles in contiguous boxes are not fully independent one from the other. As the goal of this study is to understand and model the overall kinematics of the molecular gas across the studied region rather than its very local behaviour on a scale smaller than 0.5″, this interdependence does not limit much the interpretation.

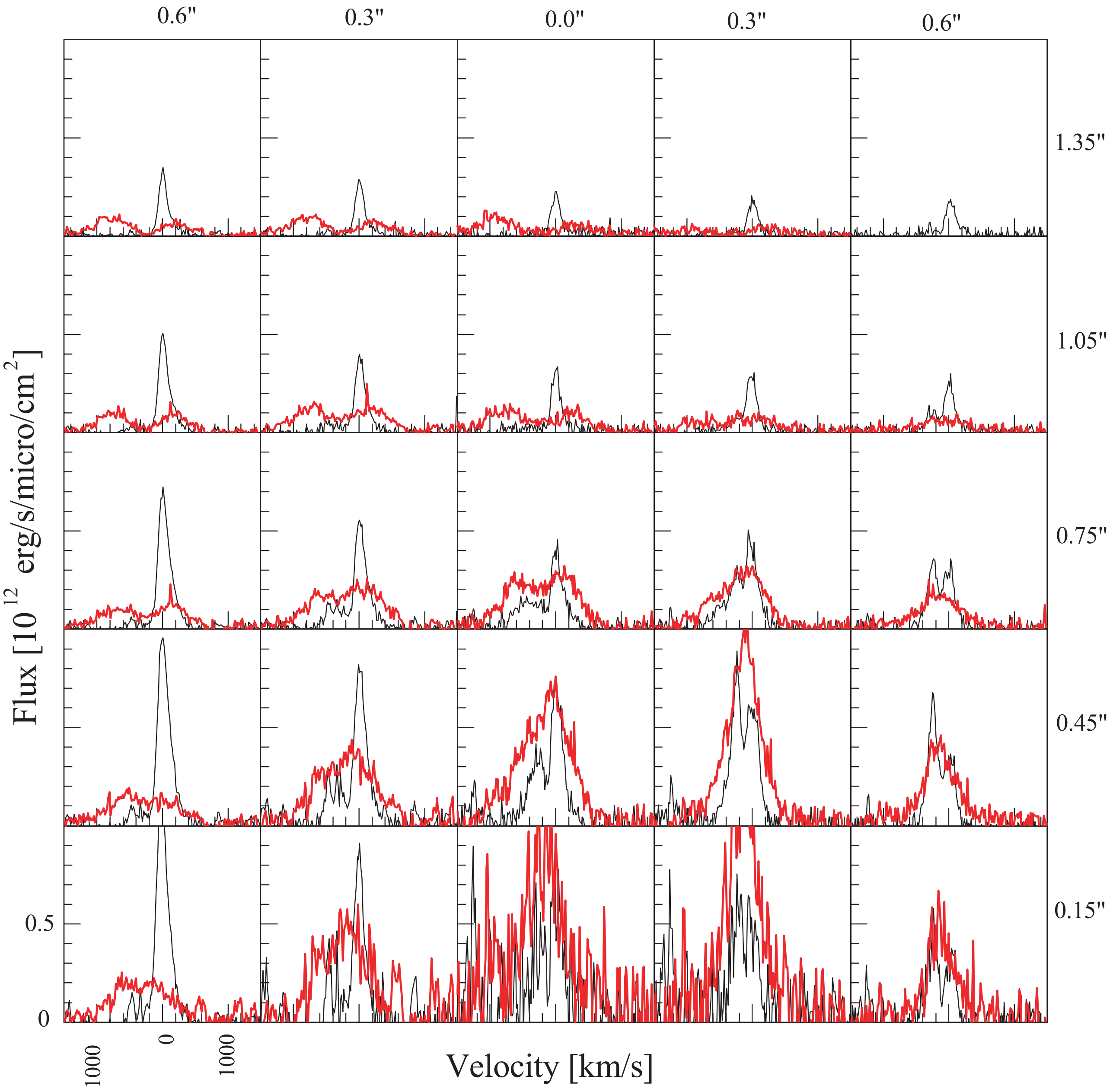

Fig. 4. The Br$_\gamma$ and H$_2$ emission line profiles across the 1.2″ × 1.2″ region to the North of the nucleus, corresponding to the North-H$_2$-Br$_\gamma$ knot. The Br$_\gamma$ line profiles are shown with a red and thick line while the H$_2$ profiles are shown with a black and thin line. Note that the X-axis velocity scale had to be changed because of much wider profiles in Br$_\gamma$ than in H$_2$. As in Fig. 3, the X-axis corresponds to PA = 102° and the Y-axis to PA = 12°. The orientation is the same as in Fig. 3.

4. Kinematics and distribution of the emitting H$_2$ material and of the ionized hydrogen over the central 4″× 4″ area

4.1. Emitting H$_2$ material and ionized hydrogen over the central 4″× 4″ area

Figure 5 summarizes some of the conspicuous facts to be concluded from these observations: superimposed over the map in the H$_2$ emission line, the contours indicate the flux in the Br$_\gamma$ emission line, while the cross features the location of the K band continuum maximum on our ISAAC data set. It has been shown by Marco et al. (1997) and Rouan et al. (1998) from AO images in the K band, that this unresolved core (less than 0.12 pc in size) is coincident, within error-bars, with the radio source S1 (central engine). The triangle shows the location of the radio source C (Muxlow et al. 1996; Gallimore et al. 1996). Marco et al. (1997) also showed that the radio source C coincides with the [OIII] emitting cloud NLR-B seen on the HST maps.

We observe that the H$_2$ line emission is not distributed uniformly around the central engine. It consists of a low level, extended and diffuse component which is minimum where the continuum is maximum (central near-IR core at (0.0″,0.0″)). In addition to this extended H$_2$ line emission, three knots which

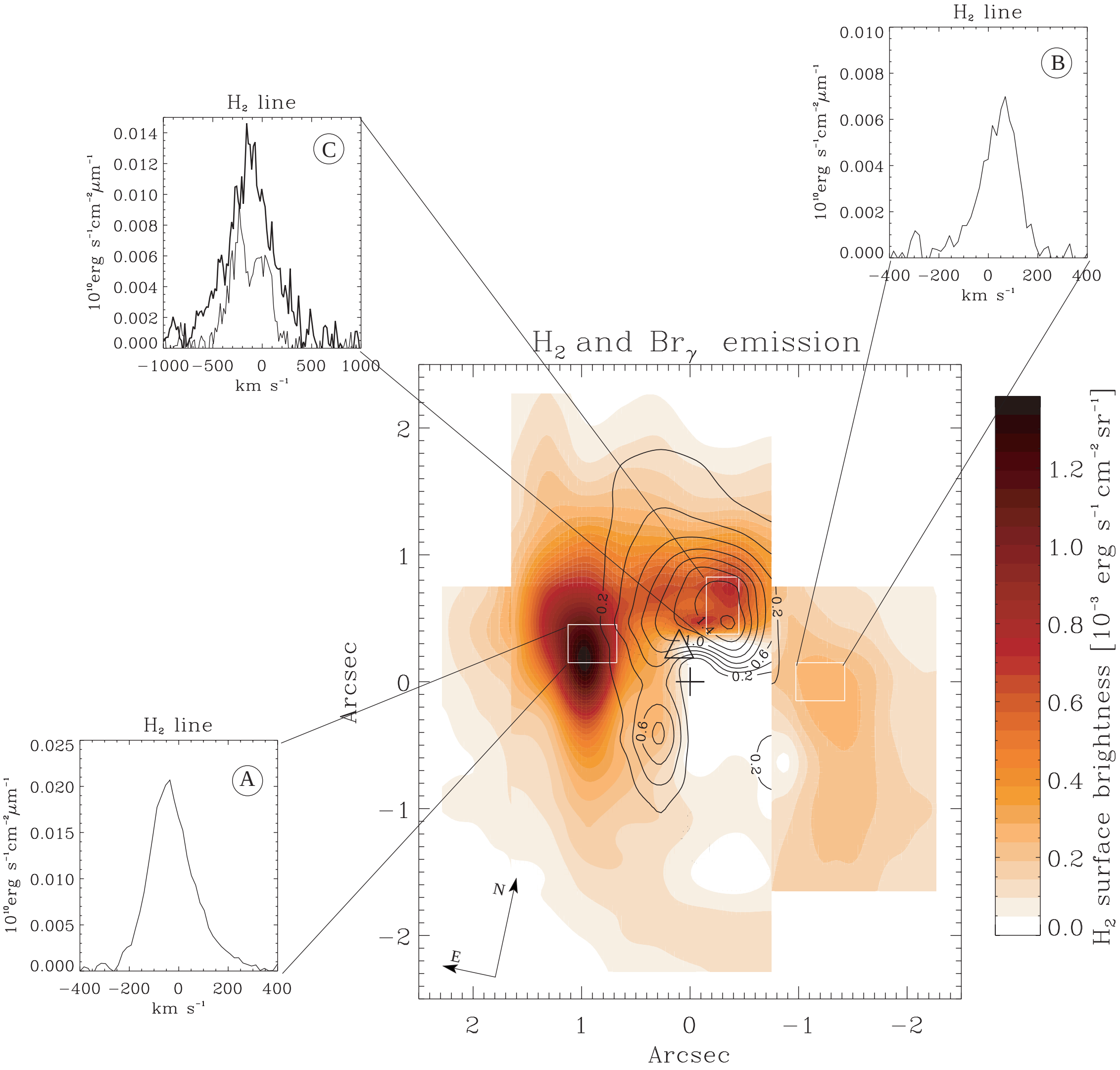

Fig. 5. Molecular and ionized gas structures in the central 4″ × 4″ of NGC 1068, as shown on a composite image made from the independent maps restored from the ISAAC data sets obtained at PA = 102° and PA = 12°. The grey-scale map corresponds to the velocity-integrated H_2 line emission. We have superimposed with black contours the Br_γ line emission which is detected mainly to the North and South of the central engine. The labels on the contours are the surface brightness in 10^{-3} erg s^{-1} cm^{-2} sr^{-1}. The cross shows the location of the central engine (position of the unresolved core seen in the *K* band continuum: its coincidence with the radio source S1 is ascertained within the error-bar of AO measurements by Marco et al. 1997). The triangle indicates the location of the radio source C. In the inserts A, B and C, we have displayed the H_2 line profiles (thick line) and the Br_γ line profile (thin line) for three particular regions, the East-H_2 knot, the North-H_2-Br_γ knot and the West-H_2 knot. The profiles are displayed on a velocity scale to allow an easy comparison: the velocity zero point corresponds to the rest wavelength of each of the lines after correction for the heliocentric recession velocity of the galaxy, 1144 ± 4 km s^{-1}, measured on our data as the mean velocity of the two sides of the suspected torus (see Sect. 4.1).

are particularly intense in the H_2 line emission have been identified: the corresponding line profiles (H_2 and/or Br_γ) are displayed in the inserts in Fig. 5. The most conspicuous one is the East-H_2 knot, well defined in position and velocity (insert A). We can isolate as well the West-H_2 knot (insert B), although it appears weaker in intensity (factor around 3). No Br_γ emission is detected at the location of the West-H_2 knot, while the East-H_2 knot does show a low level of Br_γ emission. This emission can be attributed to the wings of the strong Br_γ emission coming from the North-H_2-Br_γ knot, rather than being intrinsic to the East-H_2-knot itself. We notice that, within positional uncertainties, the East-H_2 knot and the West-H_2 knot are located almost symmetrically with respect to the position of the central engine. Their H_2 line peak velocities are respectively at 1074 ± 4 km s^{-1} and 1214 ± 4 km s^{-1}. Under the assumption that they are kinematically associated in the form of a structure rotating around the central engine, this leads to a rest velocity of the central engine of 1144 ± 4 km s^{-1}. This velocity is fully consistent with the HI heliocentric velocity of the host galaxy, 1148 ± 5 km s^{-1} (Brinks et al. 1997). In addition, the H_2 line profiles in the East-H_2 knot and West-H_2 knot have similar width and are symmetrical in shape relative to the galaxy rest velocity. The line profile of the East-H_2 knot has a blue-shifted peak and shows an extended red wing, i.e.

toward lower velocities. The line profile of the West-H_2 knot has a red-shifted peak and also displays a wing toward lower velocities (extended blue wing). The H_2 line profiles (shape and velocity) change continuously and smoothly all over the region of diffuse emission and the identified East-H_2 and West-H_2 knots: hence we can reasonably assume that they belong to a same kinematical component. The third knot identified is located to the North (insert C). It shows different characteristics than the East-H_2 knot and West-H_2 knot and emits both in H_2 and Br_γ. In this North-H_2-Br_γ knot, the H_2 line profile is double-peaked. If one considers only the red peak of the H_2 line in the North-H_2-Br_γ knot, one finds that the H_2 line profile peak velocity varies in an organized fashion from the eastern side to the western side of the central engine. Conversely, in the North-H_2-Br_γ knot, the blue-peak of the H_2 line profile is unique to this location, which is spatially coincident with the strongest Br_γ line emission detected. Although at this location the Br_γ line does not show an obvious double-peaked profile in correspondence to that observed in the H_2 line, one cannot exclude that it might be the possible blend of two components with greater *FWHM* ($\sim$700 km s^{-1}) than the H_2 line components ($\sim$190 km s^{-1}). Indeed the Br_γ line emission is expected to arise from the NLR where the presence of ionized material at high velocity is inferred from the observation of broad wings in the [OIII] line profiles (Alloin et al. 1983; Cecil et al. 1990). Let us remind finally the South-Br_γ knot which appears to be a stronger emitter in Br_γ than H_2. Notice that the Br_γ emitting knots, the North-H_2-Br_γ knot and South-Br_γ knot, are also quasi-symmetrical with respect to the central engine and outline the two sides of the ionizing cone.
From our results we can infer the following structure of the molecular and ionized material:

- The molecular H_2 line emission from (a) the diffuse component, (b) the East-H_2 knot, (c) the West-H_2 knot and (d) the red peak on the H_2 profile from the North-H_2-Br_γ knot, all arise from a same system with organized kinematical properties. This is demonstrated by the continuous spatial change of the H_2 line profile peak velocity. Within this system, the maximum velocity shift observed between the East-H_2 knot and the West-H_2 knot has a value of 140 km s^{-1}, these knots being located at a distance of $\simeq 1''$ (70 pc) on each side of the central engine. The simplest interpretation of this velocity jump is in terms of the signature of a rotating structure: under the assumption of Keplerian rotation, this implies a central mass of $10^8\ M_\odot$ (Alloin et al. 2001). Modeling of the kinematics of this system, derived from the H_2 line profile changes over the entire region, is presented in Sect. 5.
- The Br_γ line emission and the blue-peak of the H_2 line emission in the North-H_2-Br_γ knot, as well as the Br_γ emission in the South-Br_γ knot belong to a kinematically distinct system. This system is probably associated with the NLR material, as suggested by the location of the North-H_2-Br_γ knot and South-Br_γ knot, by the absence of velocity offset of their line profile peaks and by the large width of the Br_γ line. In addition, let us notice that the North-H_2-Br_γ knot is found to be close to the radio source C identified on the MERLIN map (Muxlow et al. 1996). The source C coincides with the re-direction of the small-scale radio jet (initial direction PA = 12°), possibly induced by the impact on the NLR-B cloud (for details see Bland-Hawthorn et al. 1997). The ionization resulting from the impact would explain the detection of the [OIII] and Br_γ lines.

4.2. The molecular material over the 20″ × 20″ area

The ISAAC long slit data set also provides information about the distribution of the H_2 line emission over a larger scale. The 2D spectra, particularly along PA = 12°, show weak H_2 and Br_γ emission up to almost 20″ from the nucleus on both sides. These two lines are most clearly detected between 14″ and 18″ from the nucleus to the North, and between 12″ to 17″ from the nucleus to the South. The locations of these various emission spots correspond to the star forming spiral arms clearly traced by the CO millimeter lines (Tacconi et al. 1997; Schinnerer et al. 2000). The line intensity ratio Br_γ/H_2 is about 3 to the North and 1 to the South. These lines have a *FWHM* of 35 km s^{-1} and are much narrower than the emission lines in the central 4″ × 4″ region. The spatial coverage of our data set is too scarce to extract complete 2D information over the central 40″ × 40″ where the CO arms and bar develop. Still, we notice that, along PA = 12° the presence of H_2 and Br_γ is conspicuous (Fig. 6), while these lines are rather weak along PA = 102°. Along PA = 12°, the velocity curve does not exhibit a simple behaviour. Along PA = 102° the velocity curve traced by H_2 and Br_γ is consistent with a logarithmic potential: zero on the nucleus and then rising up to a plateau.

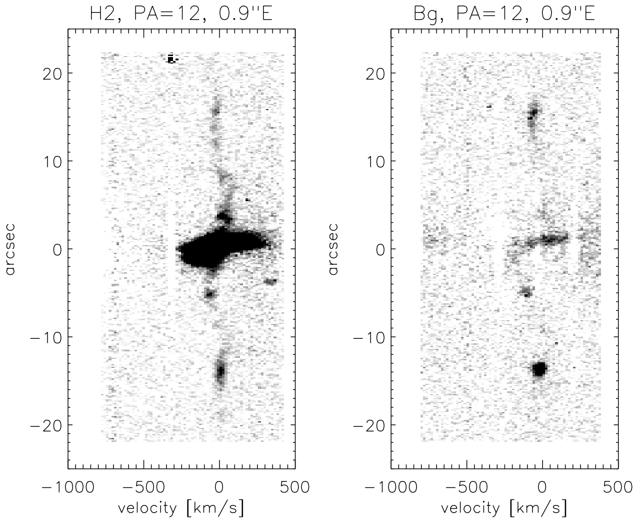

Fig. 6. Extended H_2 and Br_γ emission up to 15″ from the nucleus and with the slit passing through the East-H_2 knot. The left and right figures display respectively the $(P-V)$ diagram for H_2 and for Br_γ, along PA = 12°.

5. Kinematics: A rotating disk and an outflow

An important constraint on the kinematics of the molecular material around the central engine in NGC1068 comes from the velocity jump of 140 km s^{-1} between the East-H$_2$ and the West-H$_2$ knots. An ad-hoc jet configuration along PA = 102° might produce such projected velocities; however, as the ionization cone axis and the radio emission all appear to be aligned along PA = 10°, it seems rather natural to interpret the observed molecular emission distribution and kinematics in the framework of a somewhat axisymmetrical structure located in a plane perpendicular to the axis defined at PA = 10°. Another strong constraint on the kinematics comes from the asymmetry of the observed H$_2$ line profiles. They exhibit a more extended wing on the side of their small velocities: ie. blue wing for the profiles which are redshifted with respect to the galaxy rest-frame velocity, and red wing for the profiles which are blueshifted. This observational fact must be accounted for.

5.1. Modeling the line profiles: A model with two kinematical components

The hypothesis of a rotating structure for the molecular material is tested through a simple model. The model is used to produce a grid of H$_2$ emission line profiles to be compared to the observed ones over the $4'' \times 4''$ observed region. The model allows to produce profile grids for either of two independent kinematical components and for their combination. The two kinematical components considered are: a rotating disk and an outflow, as illustrated in Fig. 7.

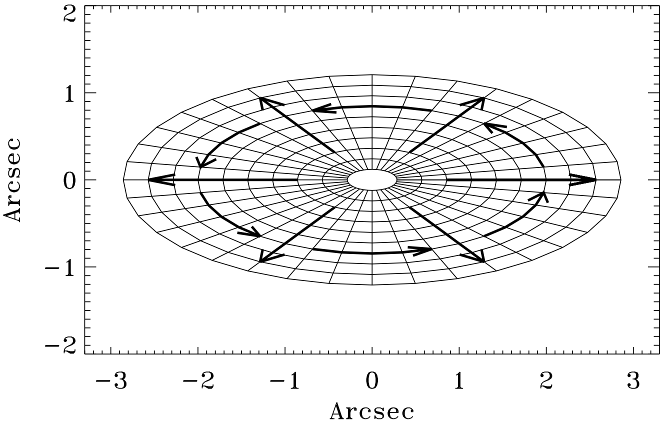

Fig. 7. Illustration of the two-component kinematical model. Arrows represent the motion of the two components.

For the rotation of the disk we assume a velocity field induced by a logarithmic gravitational potential. Such a velocity field is described by two parameters: a characteristic radius r_p and a characteristic velocity v_p. The velocity curve flattens at radii greater than r_p, and reaches a velocity v_p. The outflow is only parameterized through the outflow velocity.

The model is built in the following way: a 2D grid, where each element represents a small surface of the disk, is placed in the plane of the sky. We choose the X-axis to represent PA = 102° and the Y-axis to represent PA = 12°. 3D vectors are assigned to each element of the grid: one for the position and one for the velocity of each kinematical component. A rotation around the X-axis, to account for the inclination of the disk, is applied to these vectors. Then a v_z "image" is built for each kinematical component; we assign to each pixel of this image the along-the-line-of-sight velocity of the grid element whose projected position on the sky corresponds to the pixel position. The v_z images for a rotating and for an outflowing component are shown in Fig. 8. From each v_z image, we build a 3D cube where the third dimension is the velocity. A Gaussian profile is used to represent the emission line and is centered at the corresponding v_z value. The intensity assigned to the profiles was chosen to be constant, after checking that this assumption does not affect our conclusions. Each plane from this data cube is then convolved with a 2D Gaussian representing the point spread function (PSF) to account for seeing effects. The parameters for the kinematical model are the following:

- the velocity field parameter(s) (two parameters for the rotation and one for the outflow)
- the inclination of the disk
- the intrinsic width of the emission line for each kinematical component
- the relative intensity of the emission from each of the kinematical components

The H$_2$ line profiles predicted in the two configurations – with or without outflow – are shown in Fig. 9. We find that it is not possible to reproduce at the same time the general characteristics (asymmetry, width and peak position) of the observed H$_2$ line profiles using a model with only a rotating disk. On the contrary, the two-component model (rotating disk plus outflow) reproduces well all the profile characteristics and we shall pursue the profile fitting with such a kinematical model. Do we expect, from a modeling point-of-view, such an outflow to be present in the environment of the AGN? In classical AGN models, the observed conical funneling of the ionizing radiation field is explained by inflation of the inner part of the molecular/dusty torus. One may therefore anticipate that the impact of the X and UV photons on the edges of the inflated inner regions of the torus will sweep away material from its surface and generate an outflow.

5.2. Results

The simulated H$_2$ profiles over the $3'' \times 3''$ region are plotted on top of the observed ones in the grid shown in Fig. 10. The parameter values used to build the grid of simulated profiles matching best the observed ones, are the following:

- v_p = 100 km s^{-1}
- r_p = 50 pc
- outflow velocity: 140 km s^{-1}
- inclination angle: 65°
- *FWHM* of the rotating component: 150 km s^{-1}
- *FWHM* of the outflowing component: 200 km s^{-1}
- ratio between the line intensities emitted by the rotating and outflowing component: 2.

The modeled profiles have been scaled to peak intensity in order to allow an easier comparison among the profile shapes. The agreement between the observed and modeled H$_2$ line profiles is very good over the entire area. This validates the choice

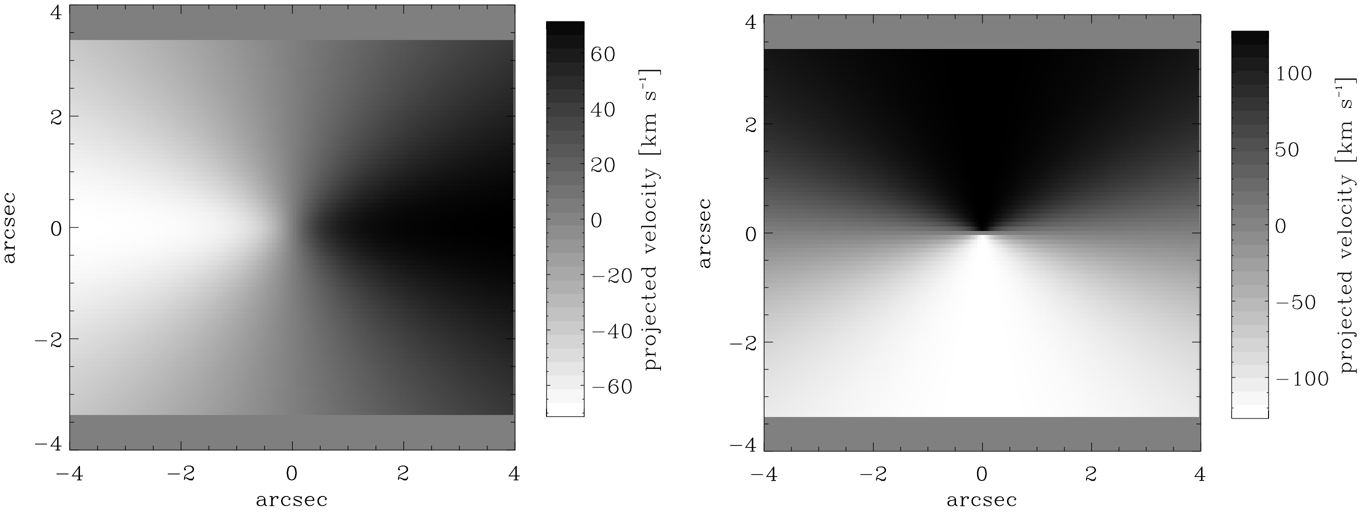

Fig. 8. Along-the-line-of-sight v_z velocity map of the rotating component (left) and of the outflow component (right) in the considered model

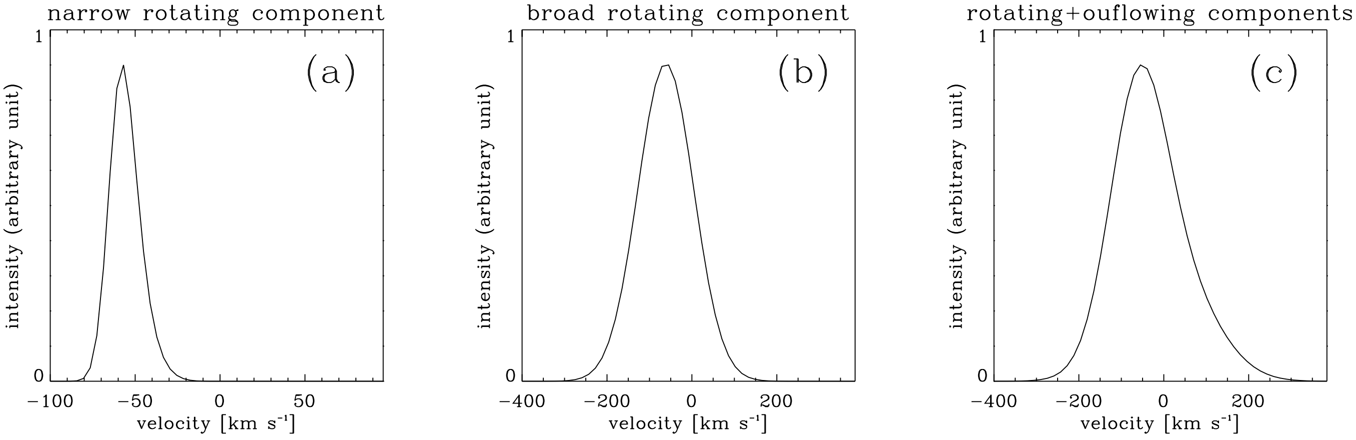

Fig. 9. Simulated profiles for the position [1″E,0″N] on the grid. From left to right: a) rotating component alone, intrinsic line *FWHM* = 15 km s^{-1} and instrumental profile not taken into account: the profile is asymmetric because of the mixture of different projected velocities resulting from the seeing. (b) rotating component alone, with intrinsic line *FWHM* = 150 km s^{-1}: the profile is symmetric because the intrinsic width is much greater than the range of projected velocities in a seeing sized-area. (c) Rotating plus outflowing components with intrinsic line *FWHM* = 150 km s^{-1} for the rotating component and line *FWHM* = 200 km s^{-1} for the outflowing component: this combination allows to reproduce at the same time the width and asymmetry of the observed profiles, as well as the spatial evolution of the asymmetry.

of a two-component kinematical model. One should note however that the figures derived for the model parameters are not constrained in a unique manner and some variation around the quoted figures may be expected as line profiles from other molecular transitions arising in the warm molecular gas will become accessible to observation.

In comparison, the CO data set discussed by Schinnerer et al. (2000) has been modeled in the framework of a warped disk. In the CO modeling, little emphasis has been put on fitting the CO line profiles, while in the case of the H_2 line emission, the profiles are used as strong constraints for the modeling. Let us recall in addition that low order CO transitions probe cold molecular material, while the H_2 transition studied here arises from warm molecular matter. Therefore a detailed comparison between the two types of models is hampered by the use of different constraints on one hand, and by reference to different temperature phases of the molecular material, on the other hand. We note however that the main emission knots detected in H_2 are located at positions coincident with the CO emitting knots. It is quite conceivable that the H_2 line originates at the surface of molecular clouds exposed to intense radiation fields, while the CO line arises from the denser and cooler inner part of these clouds. In such a configuration, surface-effects (wind...) would have a great impact on the shape of the H_2 line profile while not affecting the shape of the CO line profile.

6. Discussion: Source of excitation of the H_2 line

Apart from the North-H_2-Br_γ knot, the lack of strong Br_γ emission coincident with H_2 emission suggests that most of the molecular material emitting the H_2 line is not directly irradiated by UV photons which would also ionize hydrogen. Supporting a similar conclusion is the 90° angle offset between the ionization cone axis (along the South-North direction, Macchetto et al. 1994) and the predominant direction of H_2 line emission (East-West) in NGC 1068. Moreover, it has been shown

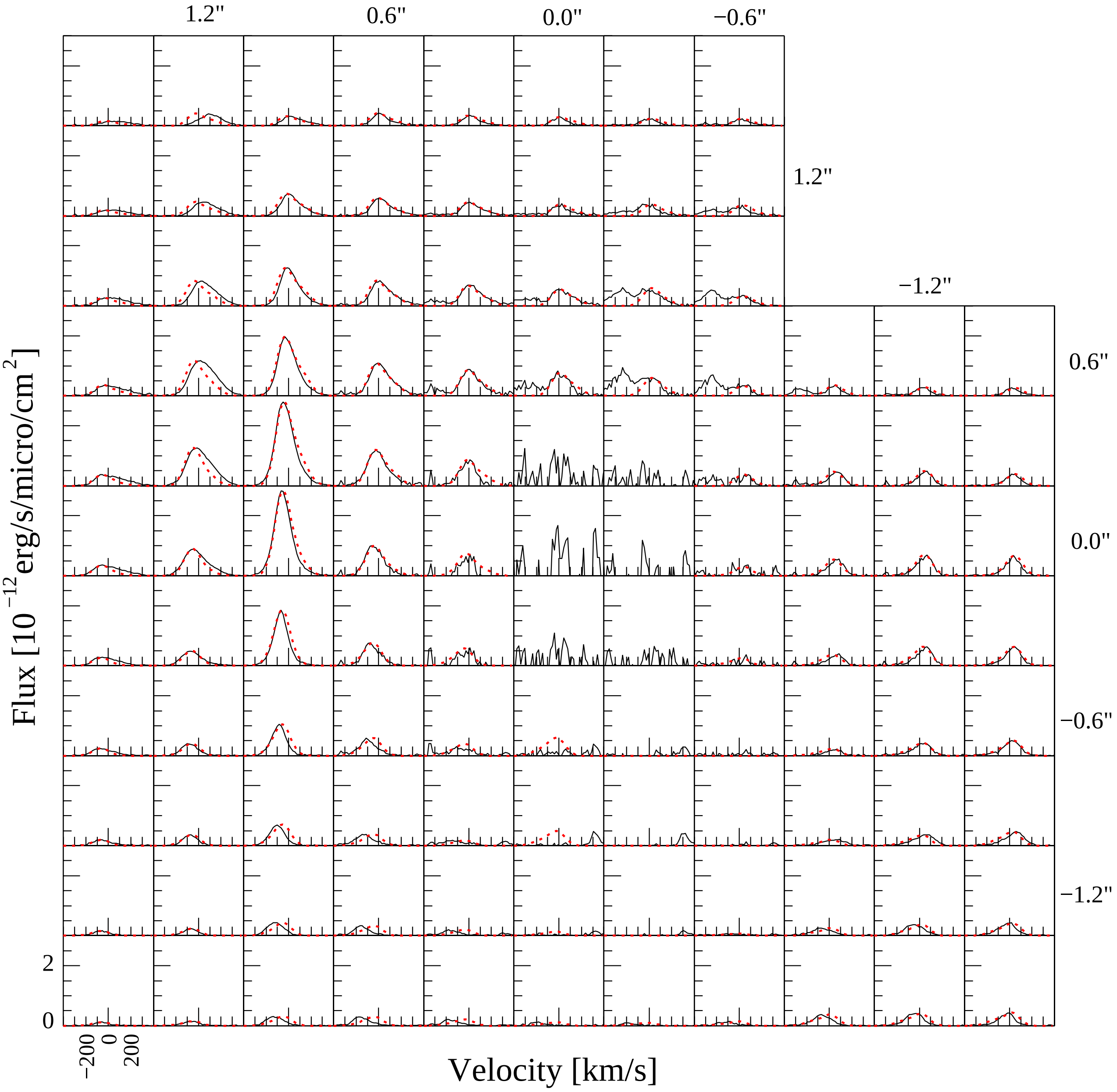

Fig. 10. Modeled profiles (dotted lines) and observed profiles (solid lines) over the $3' \times 3''$ central area. Values of the model parameters can be found in Sect. 5.2.

independently that the observed H_2 line ratio 2–1 S(1)/1–0 S(1) in NGC 1068 is consistent with thermal emission rather than with UV-pumping (Oliva & Moorwood 1990). Therefore, these three facts lead us to disregard UV photons as the source of excitation of the H_2 line in the close environment of the central engine in NGC 1068.

The remaining two possibilities to excite H_2 to the requested ~2000 K are, (a) heating by shock waves, or (b) heating due to irradiation by X-rays (Mouri 1994).

Could shocks play a dominant role in the excitation of the H_2 emission in the particular case of NGC 1068? Following Draine, Roberge & Dalgarno (1983), the shock velocities required are of the order of $V_{\rm shock} \sim$ 10–30 km s^{-1}. An order of magnitude of the total shock luminosity is given by $L_{\rm shock} \sim 1/2\,\rho_{\rm cloud}\,V^3_{\rm shock}\,A_{\rm shock}$, where $\rho_{\rm cloud}$ is the density of the cloud, $V_{\rm shock}$ the shock velocity and $A_{\rm shock}$ the total shock area (Heckman et al. 1986). A density $n_{\rm H_2} = 10^5$ cm^{-3}, a shock velocity $V_{\rm shock} = 30$ km s^{-1} and a shock area $A_{\rm shock} = 2\pi r^2_{\rm cloud}$ for $r_{\rm cloud} = 20$ pc are reasonable values for the East-H_2 knot. The total shock luminosity for these parameters is 10^{33} erg s^{-1}. About one tenth of this luminosity is radiated through the 1-0 S(1) H_2 line. The resultant predicted luminosity in this line is thus 6 orders of magnitude below the observed 3×10^{38} erg s^{-1} emitted in the East-H_2 knot. Even if we increase generously $n_{\rm H_2}$ or $A_{\rm shock}$, the observed flux values cannot be accounted for in this way. Therefore we can disregard shock heating as the source of excitation of the H_2 line around the central engine in NGC 1068.

Maloney (1997) has already discussed the X-ray irradiation of molecular clouds by the central X-ray source in NGC 1068.

His model was computed for an intrinsic 1-100 keV luminosity of 10^{44} erg s^{-1} for the central engine and an attenuating column density of 10^{22} cm^{-2} between the central engine and the H_2 emitting molecular clouds. With this set of parameters, his model accounts for the observed H_2 intensity and predicts the right size-scale of the H_2 line emission. However, Matt et al. (1997) have shown that the opaque material which obscures our direct view to the central engine of NGC 1068 is Compton thick ($N_{\rm H} \geq 10^{24}$ cm^{-2}). If this opaque material has a more or less toroidal distribution – as suggested by the existence of the ionizing cone –, then the column density between the central engine and the molecular material found at the location of the East and West-H_2 knots must also be of the order of at least 10^{24} cm^{-2}. In such a configuration, the model predicts an H_2 emission arising much closer to the nucleus than the observed 70 pc. An alternative possibility is that the azimuthal density distribution in the torus is such that the opening angle for the X-rays is larger than for the UV radiation. This situation is likely to occur since X-rays can penetrate much larger column densities than UV photons, implying that the viewing angle range over which the torus is Compton thick is smaller than the viewing angle range over which it is UV-opaque. Still, in such a situation, the H_2 emitting clouds must be located within the aperture of the cone inside which the X-rays can escape. This suggests that the molecular clouds located at a distance of 70 pc (where the H_2 emission is mainly detected) are not strictly orbiting in the plane perpendicular to the axis of the opaque torus. Consequently, either the H_2 emitting material is a component distinct from the torus and is simply orbiting in the plane of the galaxy (inclination ~40°), or we are dealing with a single disk structure within which the inclination of the plane where the molecular material orbits, changes continuously with radius: in other words the disk is warped.

The presence of a warped structure in the AGN of NGC 1068 has also been proposed by Baker (2000) to fit both the intensities and the kinematics of the CO emitting material. Interestingly, as shown in a theoretical work by Quillen (2001), a wind blowing across a dense, thin and initially flat rotating disk would automatically generate a warp. This suggests that there is a possible physical connexion between the warp and the outflow, hence between the observed distribution of H_2 emission and the H_2 line profile shapes. First, the asymmetry of the profiles witnesses the presence of an outflow. Second, modeling predictions tell us that this wind would have naturally induced a warp of the molecular disk. Third, it is the existence of the warp which makes possible the irradiation of the molecular material by the central X-rays. In summary, this scenario makes the wind the indirect cause of the H_2 emission being observed at a rather large distance from the central engine.

7. Concluding remarks

We have provided in this paper a comprehensive study of the kinematics of the warm molecular material in the environment of the AGN in NGC 1068. New runs of 2D spectroscopic observations (ISAAC on VLT/ANTU), obtained under very good seeing conditions, have complemented the data set discussed earlier by Alloin et al. (2001). The achieved spectral (35 km s^{-1}) and spatial (0.5″) resolutions allow to recover emission maps in the H_2 and Br_γ emission lines, at respective rest wavelengths 2.122 and 2.166 μm, over the central 4″ × 4″ region surrounding the central engine in NGC 1068. In addition, one witnesses the spatial evolution of the H_2 and Br_γ line profiles over the inner 3″ × 3″ region with a spatial sampling of 0.3″ × 0.3″.

The H_2 and Br_γ line emission maps and profile spatial evolution have been used to analyze the distribution and kinematics of the warm molecular gas across the 200 pc central region. The salient results of this work are the following:

- There is no detectable H_2 emission at the location of the strong 2.2 μm continuum core (which is known already to be almost coincident with the central engine), while two main regions of H_2 emission, East-H_2 and West-H_2, are detected at about 70 pc on each side of the central engine along PA = 90°, with a projected velocity difference of 140 km s^{-1}: this velocity jump is interpreted at first order as the signature of a rotating structure. Under this assumption, the systemic velocity of the AGN is found to be 1144 ± 4 km s^{-1}. No strong Br_γ emission is detected at the location of these knots. The East-H_2 knot is about three times brighter in H_2 line emission than the West-H_2 knot
- One detects as well a diffuse and extended H_2 emission, although at low intensity level. At about 0.3″ to the North of the central engine, the H_2 emission also coincides with a Br_γ line emitting knot. This North-H_2-Br_γ knot is close to the radio knot C and the brightest [OIII] cloud, NLR-B, although not exactly spatially coincident with them.
- To the South, another Br_γ line emitting region is observed, although weaker in intensity, the South-Br_γ knot. The North-H_2-Br_γ knot and South-Br_γ knot are almost symmetrical with respect to the central engine and appear to be located on the inner edges of the ionizing cone.
- The observed changes in the H_2 line profile across the 200 pc central region cannot be reproduced by the simple, disk-like, kinematical structure which matches the velocity jump between of the East-H_2 knot and the West-H_2 knot. A possible solution is to add an outflow at the surface of the rotating disk-like structure. The main parameters of the complete kinematical model are: a rotational velocity around 100 km s^{-1} at a characteristic radius of 50 pc, an inclination angle of the disk-like structure of 65° and an outflow velocity of 140 km s^{-1}.
- The source of excitation of the H_2 line is briefly discussed. Both UV photons and shocks can be discarded as the main source of excitation of the H_2 line, while X-ray irradiation from the central engine is found to be the most likely mechanism.
- An additional consequence of an outflow at the surface of a rotating disk-like structure is the occurrence of a warp. This warp does naturally explain how the X-rays can impact the molecular disk at a distance as large as 70 pc and give rise to the two observed main knots emitting H_2.

Acknowledgements. We are gratefully indebted to the ESO Service Observing team on Paranal, especially to Jean-Gabriel Cuby and Olivier Marco who performed the service mode observations, and to the User Support Group and Archive Support Group at ESO/Garching for efficient help. We acknowledge precious advice from Chris Lidman for data reduction and interesting discussions with Andrew Baker and Michael Burton. Finally, we thank the anonymous referee for stimulating remarks.

References

Alloin, D., Galliano, E., Cuby J.-G., et al. 2001, A&A, 369, L33

Alloin, D., Pelat, D., Boskenberg, A., & Sargent, W. 1983, ApJ, 275, 493

Baker, A. 2000, Molecular Gas in Nearby Active Galactic Nuclei, Ph.D. Thesis

Bland–Hawthorn, J., Gallimore, J., Tacconi, L., et al. 1997, Ap&SS, 248, 9

Blietz, M., Cameron, M., Drapatz, S., et al. 1994, ApJ, 421, 92

Bock, J., Neugebauer, G., Matthews, K., et al. 2000, AJ, 120, 2904

Brinks, E., Skillman, E., Terlevich, R., & Terlevich, E. 1997, Ap&SS, 248, 23

Capetti, A., Maccheto, F., & Lattanzi, M. 1997, ApJ, 476, L67

Cecil, G., Bland, J., & Tully, R. 1990, ApJ, 355, 70

Cuby, J.-G., Devillard, N., Jung, Y., Lidman, C., & Rogon, T. 2000a, ISAAC-SW Data Reduction Guide 1.1

Draine, B., Roberge, W., & Dalgarno, A. 1983, ApJ, 264, 485

Efstathiou, A., & Rowan-Robinson, M. 1994, MNRAS, 212, 218

Gallimore, J., Baum, S., O'Dea, C., & Pedlar, A. 1996, ApJ, 458, 136

Gallimore, J., Baum, S., & O'Dea, C. 1997, Nature, 388, 852

Glass, I. 1997, Ap&SS, 248, 191

Granato, G. L., & Danese, L. 1994, MNRAS, 268, 235

Granato, G.-L., Danese, L., & Franceschini, A. 1997, ApJ, 486, 147

Hall, D., Kleinmann, N., & Ridgway, S. 1981, ApJ, 548, 898

Helfer, T., & Blitz, L. 1995 ApJ, 450, 90

Heckman, T., Beckwith, S., Blitz, L., et al. 1986, ApJ, 305, 157

Krolik, J. 1999, Active Galactic Nuclei (Princeton University Press)

Krolik, J., & Begelman, M. 1986, ApJ, 308, L55

Machetto, F., Capetti, A., Sparks, W., et al. 1994, ApJ, 435, L15

Maloney, P. 1997, A&SS, 248, 105

Marco, O., Alloin, D., & Beuzit, J. L. 1997, A&A, 320, 399

Marco, O., & Alloin, D. 2000, A&A, 353, 465

Matt, G., Guainazzi, M., Frontera, et al. 1997, A&A, 325, L13

Moorwood, A., Cuby, J.-G., Ballester, P., et al. 1999, The Messenger, 95, 1

Mouri, H. 1994, ApJ, 427, 777

Muxlow, T., Pedlar, A., Holloway, A., et al. 1996, MNRAS, 278, 854

Oliva, E., & Moorwood, A. 1990, ApJ, 348, L5

Peterson, B. 1994, in ASP Conf. Ser., 69, 1

Pier, E., & Krolik, J. 1993, ApJ, 418, 673

Quillen, A. 2001, ApJ, 563, 313

Rotaciuc, V., Krabbe, A., Cameron, M., et al. 1991, ApJ, 370, L23

Rouan, D., Rigaut, F., Alloin, D., et al. 1998, A&A, 339, 687

Rousselot, P., Lidman, C., Cuby, J.-G., et al. 2000, A&A, 354, 1134

Schinnerer, E., Eckart, A., Tacconi, L., et al. 2000, ApJ, 533, 850

Tacconi, L., Gallimore, J., Genzel, R., et al. 1997, Ap&SS, 248, 59

Thatte, N., Quirrenbach, A., Genzel, R., et al. 1997, ApJ, 490, 238

Thompson, R., Lebofsky, M., Rieke, G. 1978, ApJ, 222, L49

Thompson, R., Chary, R.-R., Corbin, M., et al. 2001, ApJ, 558, L97

Tomono, D., Doi, Y., Usuda, T., Nishimura, T. 2001, ApJ, 557, 637

Wittkowski, M., Balega, Y., Beckert, T., et al. 1998, A&A, 329, L45